Mechanics of Materials 14 (1993) 207–221
Elsevier

Mechanics of the fiber pushout test

C. Liang and J.W. Hutchinson

Division of Applied Sciences, Harvard University, Cambridge, MA 01238, USA

Received 28 February 1992; revised version received 6 August 1992

Model equations governing the debonding and the pushout phases of the fiber pushout test are presented and are then evaluated for accuracy by comparing them with detailed numerical analyses of some specific examples. It is assumed that a residual compressive stress acts across the fiber/matrix interface and residual axial stress in the fiber is taken into account. The interface is characterized by a mode 2 debond toughness Γ and is assumed to develop a frictional stress upon sliding according to $\tau = \tau_0 - \mu\sigma_r$, corresponding to a constant stress contribution and a Coulomb term. The model applies either to pushout of a single fiber embedded in a homogeneous matrix or to a fiber selected for pushout from a specimen sliced from a fiber reinforced composite. The effect of redistribution of residual stress due to slicing the composite in preparation of the specimen is addressed in numerical examples. The detailed numerical work establishes that the debond crack advancing down the fiber becomes unstable and breaks through to the bottom of the specimen when the debond tip reaches a distance about one and one half fiber radii from the bottom. The model equations provide a reasonably accurate description of the dependence of the pushout test on its many parameters.

Notation

R_f	fiber radius
R_0	specimen radius
R_b	inner radius of support base
ρ	fiber area fraction for a specimen cut from a composite
l	length of mode 2 debond crack
t	specimen thickness
E_f, E	Young's moduli of fiber and outer region
E_1	Modulus quantity for interface crack (Eq. (2.10))
ν_f, ν	Poisson's ratios of fiber and outer region
n_R	residual compressive stress acting across fiber/matrix interface
p	compressive pushout stress applied to fiber end
p_i	pushout stress to initiate debonding
p_R	residual compressive axial stress in fibers
G	energy release rate of debond crack
$\Gamma \equiv G_c$	mode 2 debond toughness of interface
K	mode 2 stress intensity factor for debond crack
$K_c \equiv \sqrt{E_1\Gamma}$	mode 2 debonding intensity toughness of interface
U	load point displacement conjugate to p
u	displacement of fiber end relative to specimen surface

Correspondence to: Prof. J.W. Hutchinson, Division of Applied Sciences, Harvard University, 316 Pierce Hall, 29 Oxford Street, Cambridge, MA 02138, USA.

1. Introduction

Fiber pushout tests are now commonly carried out with the purpose of measuring the fiber/matrix interface debonding and frictional sliding characteristics for a wide variety of fiber reinforced composite systems (see Kearns and Parthasarathy (1991) and Marshall (1992) for a listing of references). To infer these interface

characteristics it is necessary to make certain assumptions about the nature of the laws governing debonding and friction and to then carry out a mechanics analysis of the specimen subject to these assumptions. In this way, theoretical predictions for the specimen can be fit to measured records of pushout load versus displacement using the desired interface properties as fitting parameters. The number of geometric parameters characterizing the specimen and material parameters characterizing the composite is quite large (see the Notation), and it is essential that the mechanics solution for the specimen be in closed form, rather than numerically generated for each set of parameters, if it is to be broadly useful. At the same time, it is essential that the analytical solution, which is of necessity of an approximate nature, be assessed for its accuracy. The approach taken in this paper is to present a closed form analytical solution in Section 2, which contains all the parametric dependencies and which is valid for a reasonably general friction law, and then in Sections 3 and 4 provide a full finite element analysis of the specimen for some specific cases to assess the accuracy of the analytical model results. The analytical model results coincide in almost all respects to solutions presented recently by Kearns and Parthasarathy (1991) and Marshall (1992) for the special case of Coulomb friction acting on the fiber/matrix interface.

The slicing process used to produce specimens from a composite is illustrated in Fig. 1, and the geometry of the specimen is also detailed in this figure. It is assumed that there are residual compressive stresses p_R and n_R in the axial and radial directions, respectively, in the fibers in the composite *prior to slicing*. The slicing process redistributes these residual stresses in the vicinity of the fiber ends, and one of our objectives will be to assess the effect of this redistribution on the pushout test with the aid of the numerical calculations. In many specimens, the thickness t is chosen to be not more than, typically, 6 to 12 times the fiber radius R_f so that unduly large pushout forces can be avoided. For such 'thin' specimens it is essential that the inner support radius of the base, R_b, be small enough such that significant effects due to bending do not arise (Kallas et al., 1991). If R_b is taken to be less than, say, $2R_f$, then bending effects are negligible

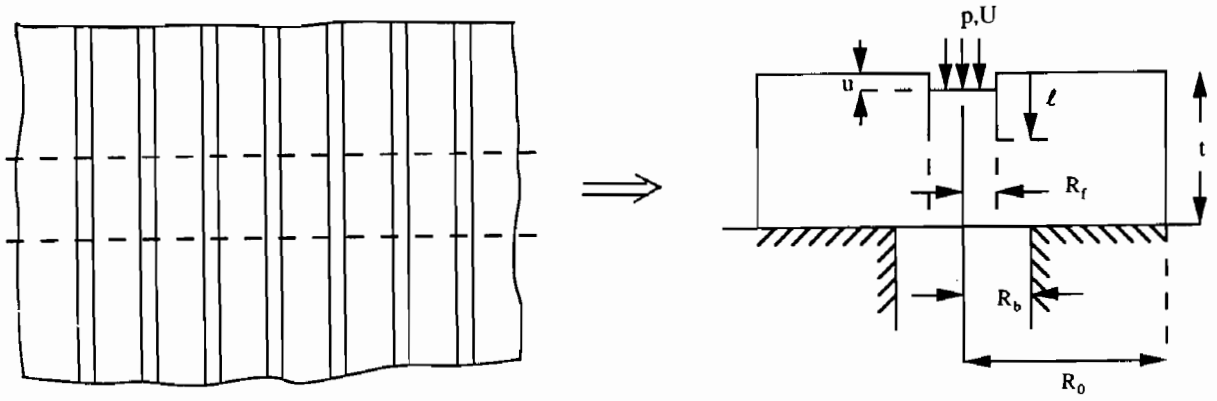

Fig. 1. Residual stresses in composite and slicing to make a specimen. Definition of length quantities for specimen.

and, moreover, R_b itself will have little influence on the pushout results. Similarly, the outer radius of the specimen R_0 plays essentially no role as long as it is more than several times t. The numerical results reported below also indicate that the details of the support conditions at the base (e.g., zero friction versus clamped) have relatively little influence, and clamped conditions will be used in most of the numerical calculations. Assumptions about the details of the fiber/matrix interface will be detailed below. The interface is assumed to be characterized by a mode 2 debond toughness (work of fracture) Γ or, equivalently, by a critical mode 2 interface intensity toughness K_c. A generalized friction law which combines the Coulomb law with a constant friction stress is used to describe the tractions exerted across the debonded interface behind the advancing mode 2 debond crack tip.

2. Approximate model governing pushout

The results in this section are derived from the paper by Hutchinson and Jensen (1990) wherein models for fiber pullout have been developed. The formulas below are converted to be applicable to the present pushout specimen with due regard for certain sign changes. Moreover, the separate results in that paper for cases of constant friction and Coulomb friction have been combined here according to the law

$$\tau = \tau_0 - \mu\sigma_r, \tag{2.1}$$

where τ_0 is the constant friction contribution, μ is the Coulomb friction coefficient, and $-\sigma_r$ is the compressive stress acting across the sliding fiber/matrix interface. This relation has been suggested by Mackin et al. (1992) as a phenomenological characterization which incorporates both a Coulomb component and a component independent of the compression across the interface which is thought to arise from significant asperity interaction of the kind documented in their paper and in earlier work by Jero and Kerans (1990).

2.1. Some basic equations

In specializing the results from Hutchinson and Jensen (hereafter referenced as H–J), it will be assumed that $(R_f/R_0)^2 \ll 1$ so that, in effect, the specimen in Fig. 1 has an infinite outer radius R_0, leading to a simplification of some formulas in the earlier reference. In addition, two cases will be considered: case (i), an isotropic fiber surrounded by an isotropic outer region; and case (ii), a transversely isotropic fiber surrounded by a transversely isotropic outer region, where the outer region can be assigned the effective elastic properties of the composite from which the specimen is sliced. The model of H–J, like that of Gao et al. (1988), uses the Lamé solution to characterize the radial dependence of the stress distribution in the fiber and the matrix at each position z through the specimen. The approach is not accurate when the mode 2 debond crack tip is within about one fiber radius from the top or bottom faces of the specimen, as will be clear in the next section where comparisons with accurate numerical solutions will be made. However, the approach is quite accurate when the crack tip is in the interior of the specimen, and it can be used to analyze the most important aspects of pushout behavior.

There are two combinations of the elastic properties, B_1 and B_2, which re-appear throughout the paper. These arise in the following relations from the Lamé solution (cf., H–J, Eq. (22))

$$(\sigma_r^- - \sigma_r^+) = B_1(\sigma_f^- - \sigma_f^+) \tag{2.2a}$$

and

$$(\epsilon_f^- - \epsilon_f^+) = B_2(\sigma_f^- - \sigma_f^+)/E_f, \tag{2.2b}$$

where σ_f and ϵ_f are the average axial stress and strain in the fiber, σ_r is the radial stress acting across the interface, and the '+' denotes values well below the debond crack tip while the '−' labels values above the tip. These relations follow from the supposition that the changes in stress distribution from one section along the fiber to another are characterized by the Lamé solution, together with imposition of continuity of normal displacement and normal traction across the in-

terface as discussed more fully in H–J. The formulas for B_1 and B_2 for the two cases are given as follows.

Case (i): isotropic fiber and isotropic outer region. Let E_f and ν_f denote the Young's modulus and Poisson's ratio of the fiber and let E and ν denote the corresponding quantities for the outer region. Then,

$$B_1 = \frac{\nu_f E}{(1-\nu_f)E + (1+\nu)E_f} \tag{2.3}$$

and

$$B_2 = 1 - 2\nu_f B_1 = \frac{(1+\nu_f)(1-2\nu_f)E + (1+\nu)E_f}{(1-\nu_f)E + (1+\nu)E_f}. \tag{2.4}$$

(In this paper B_1 is the new notation for b_1 in H–J, while B_2 replaces $b_2 E_f/E$, in each case for the limit with R_f/R_0 approaching zero. See the end of the Appendix for errata for the H–J paper.)

Case (ii): transversely isotropic fiber and transversely isotropic outer region. Let the 1-direction be aligned with the fiber axis. The relevant components of stress and strain for an elastic material with transverse isotropy with respect to the 1-axis are related by

$$\epsilon_1 = \frac{1}{E}\sigma_1 - \frac{\nu}{E}(\sigma_2 + \sigma_3), \tag{2.5a}$$

$$\epsilon_2 = -\frac{\nu}{E}\sigma_1 + \frac{1}{E^r}\sigma_2 - \frac{\nu^r}{E^r}\sigma_3, \tag{2.5b}$$

$$\epsilon_3 = -\frac{\nu}{E}\sigma_1 - \frac{\nu^r}{E^r}\sigma_2 + \frac{1}{E^r}\sigma_3. \tag{2.5c}$$

With a subscript f denoting quantities associated with the fiber and unsubscripted quantities for the outer region, the expressions for B_1 and B_2 generalize to

$$B_1 = \frac{\nu_f E^r}{(1-\nu_f^r)(E_f/E_f^r)E^r + (1+\nu^r)E_f}, \tag{2.6}$$

$$B_2 = 1 - 2\nu_f B_1. \tag{2.7}$$

Of the two coefficients, B_2 is generally about unity, while B_1 brings in the 'Poisson effect' and is a much stronger function of the elastic properties than B_2. For example for case (i) with $\nu_f = \nu = 1/3$, $B_1 = 0.167$ and $B_2 = 0.889$ when $E_f/E = 1$, and $B_1 = 0.0714$ and $B_2 = 0.952$ when $E_f/E = 3$. To see how case (ii) differs from case (i), consider an isotropic fiber surrounded by a composite comprising the same fibers with area fraction $\rho = 0.3$. Suppose the matrix of the composite is isotropic such that $\nu_m = \nu_f = 1/3$ and $E_f/E_m = 3$. A self-consistent theory determination of the transversely isotropic elastic properties of the composite needed to evaluate B_1 and B_2 in (2.6) and (2.7) gives $E_f/E^r = 2.215$ and $\nu^r = 0.351$ leading to $B_1 = 0.0911$ and $B_2 = 0.939$. These values can be compared with the second set of values quoted above for case (i), and it is seen that B_1 is the more sensitive of the two coefficients to the way in which the outer region is represented.

The central equations of the model are (2.1) and (2.2) along with the equation for axial equilibrium of the fiber and the equation for the energy release rate of the debond crack. The axial equilibrium equation for the fiber is

$$\frac{d\sigma_f}{dz} = -\frac{2\tau}{R_f}, \tag{2.8}$$

where z is the axial coordinate parallel to the fiber pointing upward, and the energy release rate at the mode 2 crack tip is

$$G = \tfrac{1}{4}(B_2 R_f/E_f)(\sigma_f^- - \sigma_f^+)^2. \tag{2.9}$$

This equation for G is an exact steady-state result for a free-sliding fiber ($\tau = 0$) in the interior of an infinitely thick, homogeneous isotropic matrix. For a general elastic mismatch between the fiber and the matrix in case (i), the relation between the mode 2 interface stress intensity factor K and the energy release rate is

$$G = \tfrac{1}{2}(1-\beta^2)\left(\frac{1-\nu_f^2}{E_f} + \frac{1-\nu^2}{E}\right)K^2 \equiv \frac{1}{E_I}K^2 \tag{2.10}$$

where β is the second plane strain Dundurs parameter and E_I is an interface cracking modulus conveniently representing the collection of

moduli quantities shown. (See, for example, Hutchinson and Suo (1991) for a background to the above equation and for the expression for β. For most systems of interest in the present context, β^2 is seldom larger than a few percent.)

2.2. Debonding phase

Let Γ denote the mode 2 toughness of the fiber/matrix interface, and let p_R be the compressive axial stress in the fiber prior to any debonding. (Expressions for p_R and n_R in terms of the thermal mismatch strains and the elastic properties of the composite are given by H–J.) Then imposition of the debonding criterion, $G = \Gamma$, with $\sigma_f^+ = -p_R$ and $\sigma_f^- = -p_i$ gives the compressive pushout stress in the fiber needed to start the debond moving down the interface before any appreciable frictional resistance develops,

$$p_i = p_R + 2\sqrt{\frac{\Gamma E_f}{B_2 R_f}}\,. \tag{2.11}$$

In writing this equation it has been assumed that an initial debond region of length on the order of R_f pre-exists, otherwise a larger initiation pushout stress p_i would be required, as will be made clearer in Section 4.

Once debonding has started, the debond length l increases with pushout stress p according to

$$\frac{l}{R_f} = \frac{1}{2\mu B_1}\ln\left(\frac{\tau_0 + \mu n_R + \mu B_1(p - p_R)}{\tau_0 + \mu n_R + \mu B_1(p_i - p_R)}\right), \tag{2.12}$$

where n_R is the compressive stress acting across the interface prior to any debonding. Alternative, equivalent expressions to (2.12) are

$$\begin{aligned} p &= p_R + 2\sqrt{\frac{\Gamma E_f}{B_2 R_f}}\,e^{\zeta} + \frac{\tau_0 + \mu n_R}{\mu B_1}(e^{\zeta} - 1) \\ &= p_i + \left(2\sqrt{\frac{\Gamma E_f}{B_2 R_f}} + \frac{\tau_0 + \mu n_R}{\mu B_1}\right)(e^{\zeta} - 1), \end{aligned} \tag{2.13}$$

where $\zeta = 2\mu B_1 l/R_f$. The limit to (2.12) and (2.13) for $\tau_0 = 0$ corresponding to Coulomb friction coincides with the results given by Kearns and Parthasarathy (1991) and Marshall (1992) for case (i), although the form is somewhat different. In particular, the role of the residual axial compression in the fiber p_R is transparent in the first of the formulas in (2.13) – it simply adds to the pushout stress. The second expression in (2.13) emphasizes how the debond toughness and the fraction combine to give the increment of pushout stress required over and above initiation. The limit for constant friction ($\mu = 0$) is the elementary result $l/R_f = (p - p_i)/(2\tau_0)$. Note that the above results hold for case (ii) as well when (2.6) and (2.7) are used for B_1 and B_2.

Kearns and Parthasarathy and also Marshall introduce a reference tensile stress quantity, σ_f^0, which is the stress in the debonded portion of the fiber required to reduce the radial component of the interface traction, σ_r^-, to zero. By (2.1), this quantity is related to the residual stress quantities by $n_R = B_1(\sigma_f^0 + p_R)$. If n_R is eliminated from (2.13) in favor of σ_f^0, then for the Coulomb friction limit one obtains the form which these authors give, i.e.,

$$p = -\sigma_f^0 + \left(2\sqrt{\frac{\Gamma E_f}{B_2 R_f}} + p_R + \sigma_f^0\right)e^{\zeta}. \tag{2.13a}$$

The sliding displacement of the top of the fiber relative to the matrix (see Fig. 1) is given by

$$\frac{u}{R_f} = B_2\left(\frac{p - p_i}{2\mu B_1 E_f} - \frac{(\tau_0 + \mu n_R)}{\mu B_1 E_f}\frac{l}{R_f}\right), \tag{2.14}$$

where $p - p_i$ may be expressed in terms of l/R_f using (2.11) and (2.13). Within the framework of the model, the displacement U through which p works can be approximated by u plus a contribution due to the deformation of the specimen under p in the absence of debonding. Thus,

$$\frac{U}{R_f} = \frac{u}{R_f} + C\frac{p}{E_f}\,. \tag{2.15}$$

The constant C has been evaluated using the numerical procedures of the next section. For case (i) with $\nu_f = \nu_m = 1/3$ and E_f/E in the range

1 to 5, C is well approximated by $1.46(E_f/E)^{1/2}$. The limit of (2.14) for constant friction ($\mu = 0$) is

$$\frac{u}{R_f} = \frac{2B_2 l}{R_f}\sqrt{\frac{\Gamma}{B_2 R_f E_f}} + \frac{B_2\tau_0}{E_f}\left(\frac{l}{R_f}\right)^2. \qquad (2.16)$$

In the next section, where a full numerical analysis of the specimen under constant friction conditions will be given, it will be seen that the debond crack advances stably until the crack tip reaches a distance of about $1.5R_f$ from the bottom of the specimen where it becomes unstable and breaks through to the bottom surface by dynamic advance. Let p^* and U^* denote the load and displacement associated with the point where the debond crack loses stability. A good approximation to these instability values can be obtained from the above equations by taking l to be $t - 1.5R_f$, i.e.,

$$p^* = p_R + 2\sqrt{\frac{\Gamma E_f}{B_2 R_f}}\, e^{\zeta^*} + \frac{\tau_0 + \mu n_R}{\mu B_1}(e^{\zeta^*} - 1), \qquad (2.17)$$

$$\frac{U^*}{R_f} = C\frac{p^*}{E_f} + B_2\left(\frac{p^* - p_i}{2\mu B_1 E_f} - \frac{(\tau_0 + \mu n_R)}{\mu B_1 E_f}\frac{t}{R_f}\right). \qquad (2.18)$$

Here $\zeta^* = 2\mu B_1(t - 1.5R_f)/R_f$. These two equations contain the many parameters in the pushout problem. Moreover, the three contributions to the pushout stress at break-through are clearly exposed in (2.17), respectively due to residual stress, debonding toughness and friction.

2.3. Pushout phase

After the debond tip has broken through to the bottom of the specimen the pushout force is opposed only by friction. However, the axial stress in the fiber at the bottom is now relieved with a redistribution of the compressive stress acting across the fiber/matrix interface. At the bottom after break-through, this compressive stress becomes $n_R - B_1 p_R$; which is assumed to be positive in what follows. With d as the remaining length of the fiber in the matrix ($d = t - u$), the pushout stress is

$$p = \left(\frac{\tau_0 + \mu(n_R - B_1 p_R)}{\mu B_1}\right)(e^{\zeta_d} - 1), \qquad (2.19)$$

where $\zeta_d = 2B_1\mu d/R_f$. In the limit $\mu \to 0$, this reduces to the elementary result $p = 2\tau_0 d/R_f$ implying a linear drop-off of pushout load with displacement. The limit of Coulomb friction ($\tau_0 = 0$) gives a nonlinear relation between the pushout force and displacement, i.e.,

$$p = \frac{n_R - B_1 p_R}{B_1}(e^{\zeta_d} - 1), \qquad (2.20)$$

with the force dropping more rapidly in the beginning ($d \cong t$) than at the end ($d \cong 0$). With $(n_R - B_1 p_R)$ identified as the redistributed compressive stress normal to the fiber/matrix interface at the bottom of the specimen, this formula agrees with that of Shetty (1988), who adapted the earlier pullout results of Takaku and Arridge (1973). It also agrees with equivalent formulas of Kearns and Parthasarathy (1991) and Marshall (1992), noting that the coefficient in (2.20) is just σ_f^0. Recent detailed elasticity calculations of Meda et al. (1992) have demonstrated the accuracy of this formula.

The drop in the pushout stress Δp which occurs when the debond breaks through to the bottom of the specimen is given by (2.17) minus (2.19) with $d \cong t$.

3. Numerical analysis of the specimen with constant friction τ_0 (case (i))

Attention will be restricted to pushout histories which are monotonic in the sense that the average downward displacement of the end of the fiber U is increased monotonically. The debond crack length also increases monotonically under these circumstances. An important consequence of this monotonicity for the purpose of analyzing and presenting results for the specimen is that, for a given debond crack length, the quantities K, U and u are linear functions of p, τ_0 and p_R.

(The residual compression across the fiber/matrix interface n_R plays no direct role in the constant friction solution.) Specifically, this means it is possible to write

$$K/\sqrt{R_f} = pf_1(\xi) - p_R f_2(\xi) - \tau_0 f_3(\xi), \quad (3.1)$$

$$UE_f/R_f = pg_1(\xi) - p_R g_2(\xi) - \tau_0 g_3(\xi), \quad (3.2)$$

$$uE_f/R_f = ph_1(\xi) - p_R h_2(\xi) - \tau_0 h_3(\xi). \quad (3.3)$$

The nine quantities f_i, g_i and h_i are functions of the normalized interface crack length, $\xi = l/R_f$, as well as the other dimensionless geometric and material property parameters: t/R_f, E_f/E, ν_f and ν. In addition, as discussed in the Introduction, these functions also depend very weakly on R_0/R_f, R_b/R_f and on the precise manner in which the specimen is supported on its base. The functions of ξ are plotted in Figs. 2–4 for selected values of the nondimensional parameters. The fiber and outer region are each isotropic (case (i)): $\nu_f = \nu = 1/3$; and $E_f/E = 1$ or 3. To provide a relatively severe test for the model equations, a thin specimen has been chosen with $t/R_f = 6$ but results for a thicker specimen with $t/R_f = 12$ have also been obtained and will be discussed. The results are calculated with completely clamped conditions along the base of the specimen and with $R_0/R_f = 5$ and $R_b/R_f = 1.5$. Each of the three contributions will be discussed in turn, and the effects of varying certain parameters will also be discussed. Some of the details of the finite element procedures used to solve for these functions are discussed in the Appendix. Each contribution is analyzed as a mode 2 crack problem with crack faces which slide relative to one another but whose normal opening displacement is zero. Thus, when the individual contributions are summed, the net result applies to a mode 2 problem.

The corresponding results from the model will be compared with the full numerical calculations. The model results can be obtained in a straightforward way from the basic equations of Section 2.1. They are

$$K/\sqrt{R_f} = \sqrt{\frac{B_2 E_1}{E_f}} \left(\tfrac{1}{2}(p - p_R) - \tau_0 \frac{l}{R_f} \right), \quad (3.4)$$

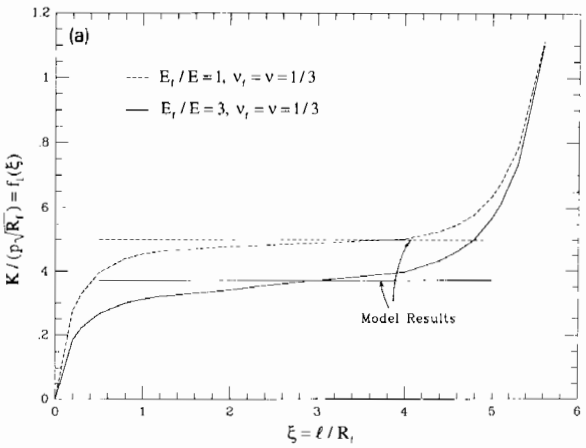

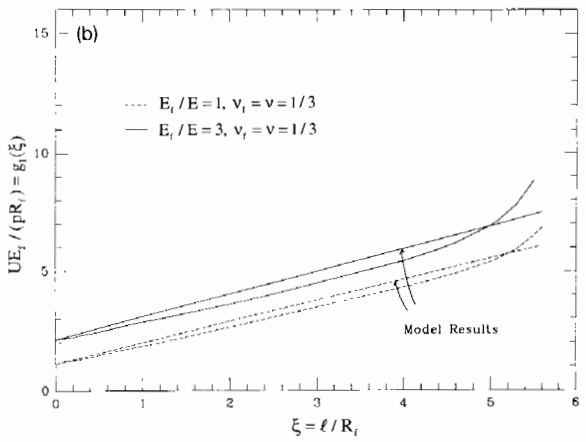

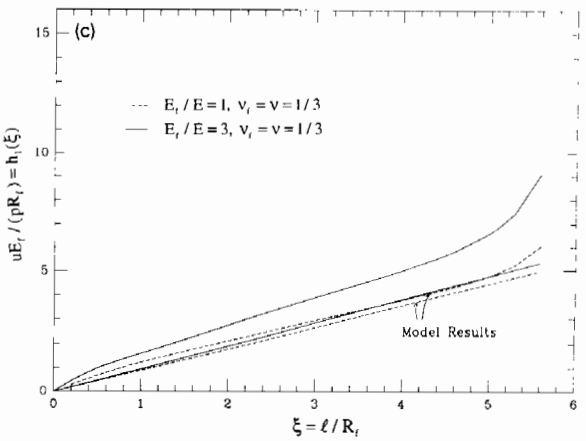

Fig. 2. Contributions due to p in Eqs. (3.1)–(3.3). The parameters of the specimen are defined in the text.

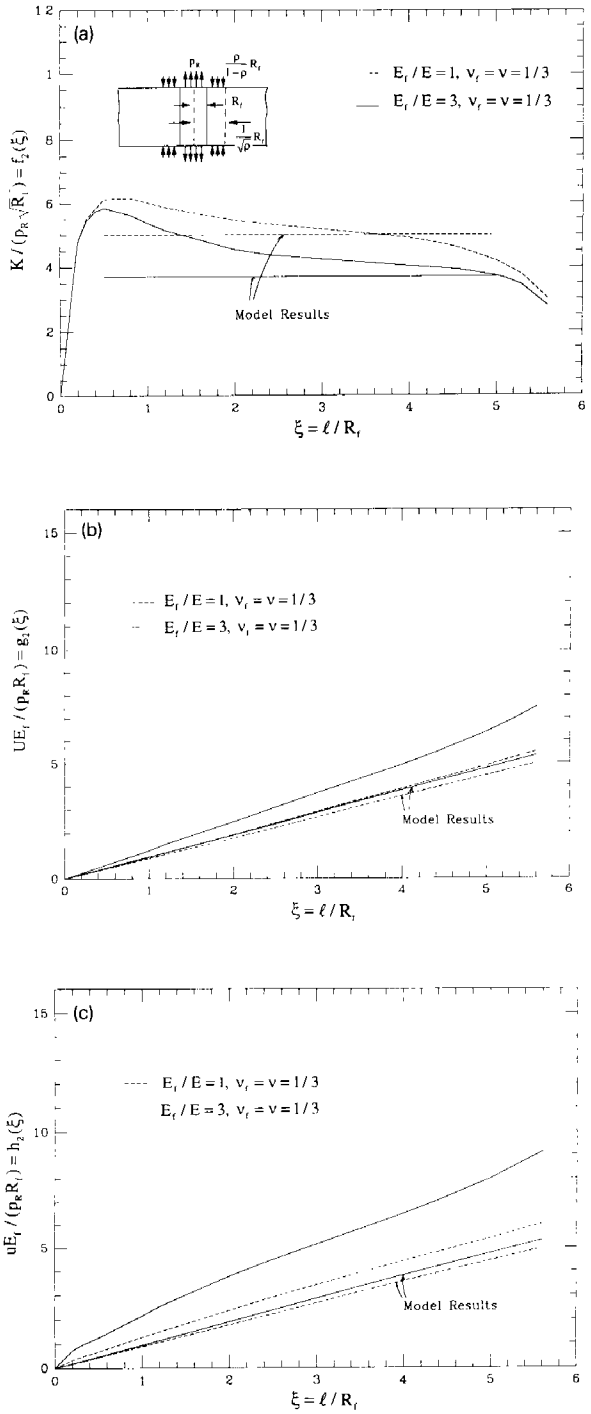

Fig. 3. Contributions due to p_R in Eqs. (3.1)–(3.3). The insert in (a) shows the tractions applied to the specimen to generate the contribution. The parameters of the specimen are defined in the text and $\rho = 4/9$.

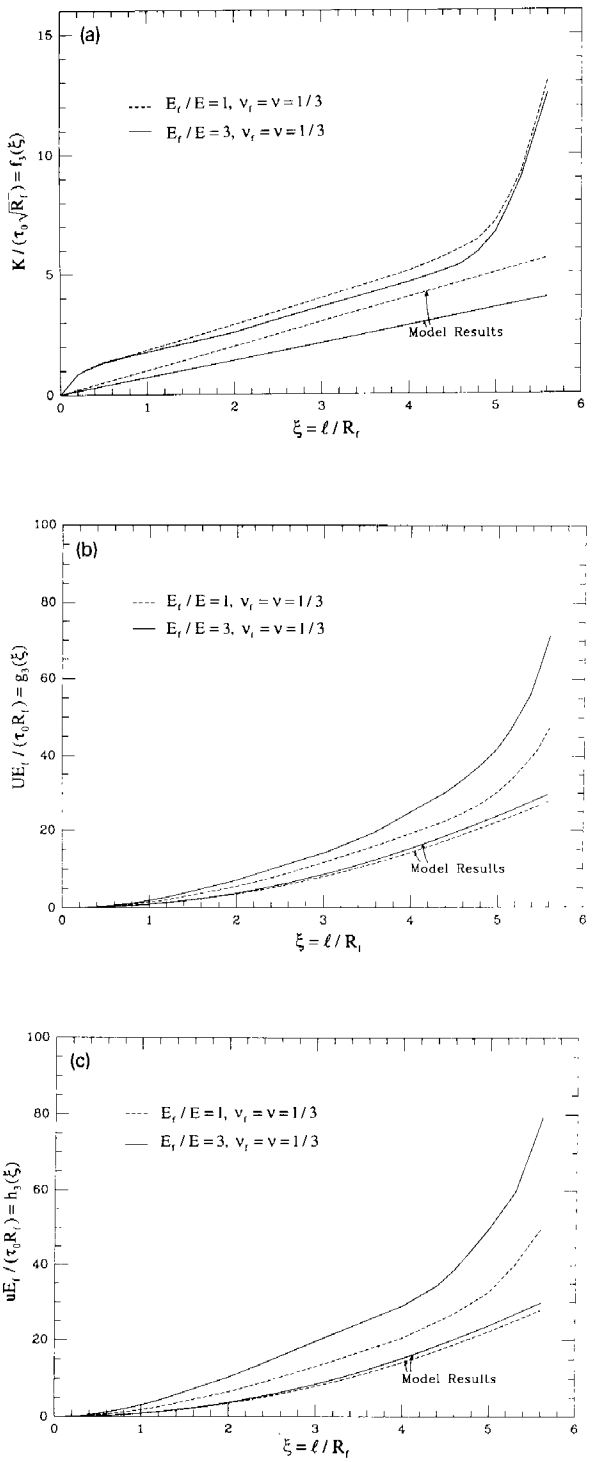

Fig. 4. Contributions due to τ_0 in Eqs. (3.1)–(3.3). The parameters of the specimen are defined in the text.

$$uE_f/R_f = B_2\left[(p-p_R)\frac{l}{R_f} - \tau_0\left(\frac{l}{R_f}\right)^2\right], \qquad (3.5)$$

with $U = u + C_p R_f/E_f$.

3.1. Contribution due to pushout stress p

The contributions to K, U and u from the pushout stress p as calculated using the finite element program are shown in Fig. 2. As just discussed, the crack is modelled as a mode 2 crack in these calculations with closed, frictionless crack faces, as is consistent with the representation in (3.1)–(3.3). Included in each of these figures are the predictions from the simple model, (3.4) and (3.5). The contribution of p to K in Fig. 2a increases sharply with crack length, reaching the 'steady-state' plateau at $\xi \cong 1$. This plateau regime persists until the crack approaches a distance of about one and one half fiber radius from the bottom of the specimen, at which point the nondimensional stress intensity factor increases dramatically as the crack breaks through to the bottom of the specimen. These features are even clearer in Fig. 5 which compares results for two specimen thicknesses, $t = 6R_f$ and $t = 12R_f$. The contribution to K for the shortest cracks and for cracks within the broad mid-region of the specimen are independent of specimen thickness. Similarly, for crack tips within about $1.5R_f$ from the bottom, the contribution to K from p is otherwise independent of specimen thickness. The result from the model obtained from (3.4) clearly applies to the plateau regime.

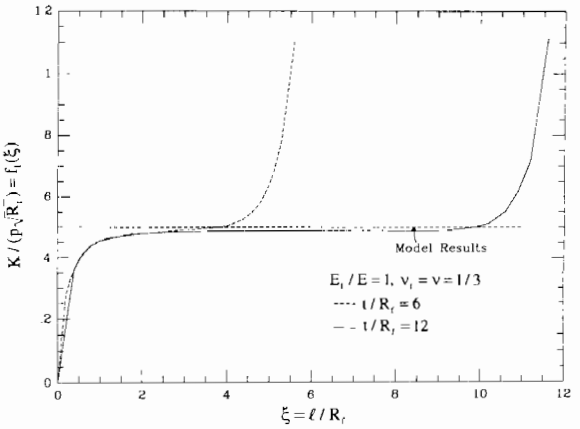

Fig. 5. Contributions to K in (3.1) due to p for two thicknesses of specimen. The parameters of the specimen are otherwise the same as those in Fig. 2a.

The contributions to U and u due to p are shown in Figs. 2b and 2c where the model predictions are also included. The constant C appearing in the model equations has been obtained from the numerical results of this section. As the crack length increases, the relative difference between U and u diminishes. The agreement with the model equations improves for thicker specimens as discussed below.

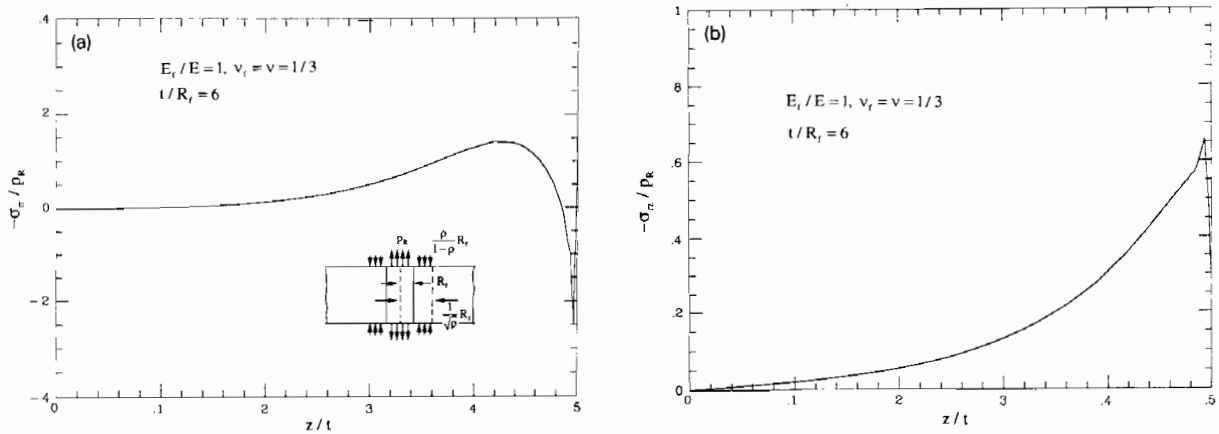

Fig. 6. Changes in normal and shear stress on the fiber/matrix interface due to slicing a specimen from a composite with an axial residual compressive stress p_R in the fiber. The insert displays the tractions applied to the specimen to model the stress changes caused by slicing. The parameters of the specimen are the same as those in Figs. 2–4 with $\rho = 4/9$, $E_f = E$ and $\nu_f = \nu = 1/3$.

3.2. Contribution due to axial residual compression p_R in the fiber, including the effect of stress redistribution due to specimen preparation

There is a significant redistribution of residual stress near the fiber ends when the specimen is sliced from the composite. Or, if a single fiber specimen is prepared with a homogeneous other matrix without slicing such that residual stresses develop in the fiber, then the stresses near the fiber ends will also be different from what they are in the interior. Here attention will be focussed on specimens sliced from a composite with fiber area fraction ρ. As discussed in the Introduction, p_R is the residual axial stress in the fibers of the composite *prior to slicing*, and the functions f_2, g_2, and h_2 in (3.1)–(3.3) reflect the redistribution resulting from the slicing process. Finite element results for the contributions due to p_R to normalized K, U and u are shown in Fig. 3. The insert in Fig. 3a shows the tractions applied to determine the contribution due to p_R. The residual stress distribution in the unsliced composite 'cell' is modeled as having a compressive stress p_R in the fiber and a tensile stress $\rho p_R/(1-\rho)$ which acts over an area weighted to correspond to the appropriate area fraction of the matrix relative to the fiber such that the total force on each of the potential top and bottom faces is zero. The slicing process then is equivalent to applying equal and opposite tractions to remove these stresses, as indicated in the insert. Plots of the *changes* in the normal and shear stresses acting on the fiber/matrix interface as calculated by this procedure are shown in Fig. 6 for the set of parameters indicated in the figure caption. The changes constitute a significant fraction of p_R but they are confined to a region a few fiber radii from the ends of the fiber.

The simplest way to compute K, U and u due to p_R is by applying the tractions shown in the insert of Fig. 3a to the specimen for each length of mode 2 crack. This is equivalent to cancelling the shear tractions acting across the interface due to introduction of the mode 2 crack. In presenting the contribution to U, $g_2(\xi)$, the very small displacement associated with $\xi = 0$ is subtracted off such that $g_2(0) = 0$.

Included in Fig. 3 are the predictions from the model from (3.5) which are seen to provide a reasonable approximation in the mid-region of the specimen. The redistribution due to slicing gives rise to a peak contribution to K due to p_R which exceeds the mid-region levels and which occurs at a crack length of just over one half a fiber radius. Since the contribution due to p_R is a negative (see Eq. (3.1)), the effect of the redistribution is to require a larger pushout stress to start the debond crack moving down from the top surface of the specimen than would otherwise be predicted. The contribution to K falls to zero as the crack approaches the bottom surface of the specimen since the axial residual stress is then largely relieved.

3.3. Contribution due to the constant friction stress τ_0

The contributions in (3.1)–(3.3) due to τ_0 are shown in Fig. 4, where the predictions from the model are also included. The model results for K in Fig. 4a underestimate somewhat the actual contribution, but the slope of the relation in the interior portion of the specimen is captured by the model. This same tendency was observed in the comparative study of pullout in Fig. 7 of H–J, where it is also seen that the accuracy of the model improves as the debond length grows (assuming it is still well away from break-through). Thus, the discrepancies between the detailed numerical results and the model seen in Fig. 4 diminish significantly in the interior of the specimen for specimens thicker than the one considered in this example, as will now be discussed.

3.4. Dependence on other parameters and support conditions

The numerical results for the choice $t/R_f = 6$ shown above provide a fairly severe test for the model equations since end effects extend into the specimen a distance of between one to two fiber radii, typically, from the free surfaces. The model equations do not incorporate end effects, yet nevertheless the model captures the quantitative trends when the debond is in the interior of the

specimen. Figure 5 illustrates the applicability of the model equations to the portion of the specimen away from the ends. Generally speaking, the model predictions for K are the more accurate than those for U, which in turn are more accurate than those for u. The calculations for $t/R_f = 12$ show a systematic improvement in accuracy of the model equations for all three quantities over those for $t/R_f = 6$. For example with $E_f = E$, the error in the model predictions at $l = t/2$ drops from 3.6 to 1.8% for K, from 9.0 to 6.7% for U, and from 27 to 17% for u. For $E_f/E = 3$, the error improvements for a specimen with $t/R_f = 12$ rather than 6 are 14.7 to 4.0% for K, 22 to 13% for U, and 55 to 26% for u.

Some of the calculations displayed above were repeated using free sliding boundary conditions (rather than completely clamped) along the bottom surface of the specimen. This alteration had virtually no effect on the numerical results for the functions in Figs. 2–4. Similarly, reducing R_0/R_f from 5 to 3 had virtually no effect.

4. Fracture analysis of the specimen with constant friction (case (i))

The equations (3.1) and (3.2) of the previous section will now be used to generate pushout load–displacement relations during the debonding phase and, consequently, to identify the point where the debond crack becomes unstable and dynamically breaks through to the bottom of the specimen. Impose the condition $K = K_c \equiv (E_I\Gamma)^{1/2}$ on Eq. (3.1) to obtain the following

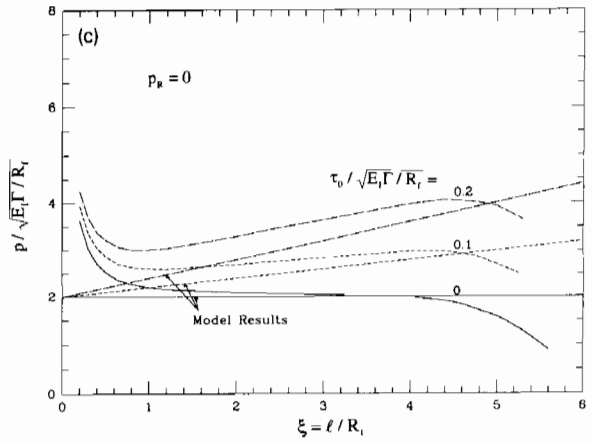

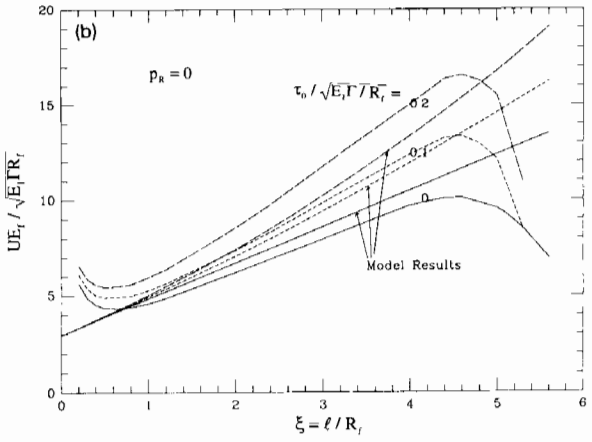

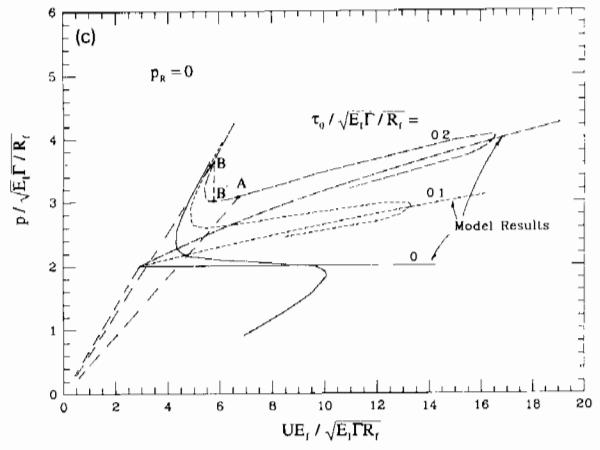

Fig. 7. Pushout behavior during the debonding phase for $p_R = 0$ with several levels of constant friction. Comparison of the full numerical results from (4.1) and (4.2) with the model predictions. In part (c) the point where $l = t - 1.5R_f$ is indicated by a dot for the model predictions. The straight line segments emanating from the origin in (c) correspond to the behavior prior to the onset of debonding as discussed in the text. The parameters of the specimen are the same as those of Figs. 2–4 with $t/R_f = 6$, $E_f = E$ and $\nu_f = \nu = 1/3$.

relation between p and the normalized debond length ξ:

$$\frac{p}{\sqrt{E_1\Gamma/R_f}} = \frac{1}{f_1(\xi)}\left(1 + \frac{p_R}{\sqrt{E_1\Gamma/R_f}} f_2(\xi) + \frac{\tau_0}{\sqrt{E_1\Gamma/R_f}} f_3(\xi)\right). \quad (4.1)$$

Equation (3.2) with (4.1) supplies U as a function of ξ according to

$$\frac{UE_f}{\sqrt{E_1\Gamma R_f}} = \frac{p}{\sqrt{E_1\Gamma/R_f}} g_1(\xi) - \frac{p_R}{\sqrt{E_1\Gamma/R_f}} g_2(\xi) - \frac{\tau_0}{\sqrt{E_1\Gamma/R_f}} g_3(\xi). \quad (4.2)$$

Examples are shown in Fig. 7 where the f's and g's are those plotted in Figs. 2–4 for the case with $E_f = E$, $\nu_f = \nu = 1/3$, and $t/R_f = 6$. Figure 7 isolates the effect of friction showing results for several values of the nondimensional friction parameter, in every case with $p_R = 0$. Plots a and b of this figure display the dependence of p and U, respectively, on ξ, while ξ has been eliminated in plot c with p cross-plotted against U. The curves in these plots apply when the debond condition, $K = K_c$, is met. The straight lines emanating from the origin have been added to indicate behavior prior to any debond crack advance, as will be discussed below. Included in each of the three plots of Fig. 7 are predictions of the model for precisely the same case. The model predictions are given by (2.13) and (2.15) for the limit $\mu = 0$. Equivalently, they can be obtained from (3.4) and (3.5) after $K = K_c$ is imposed.

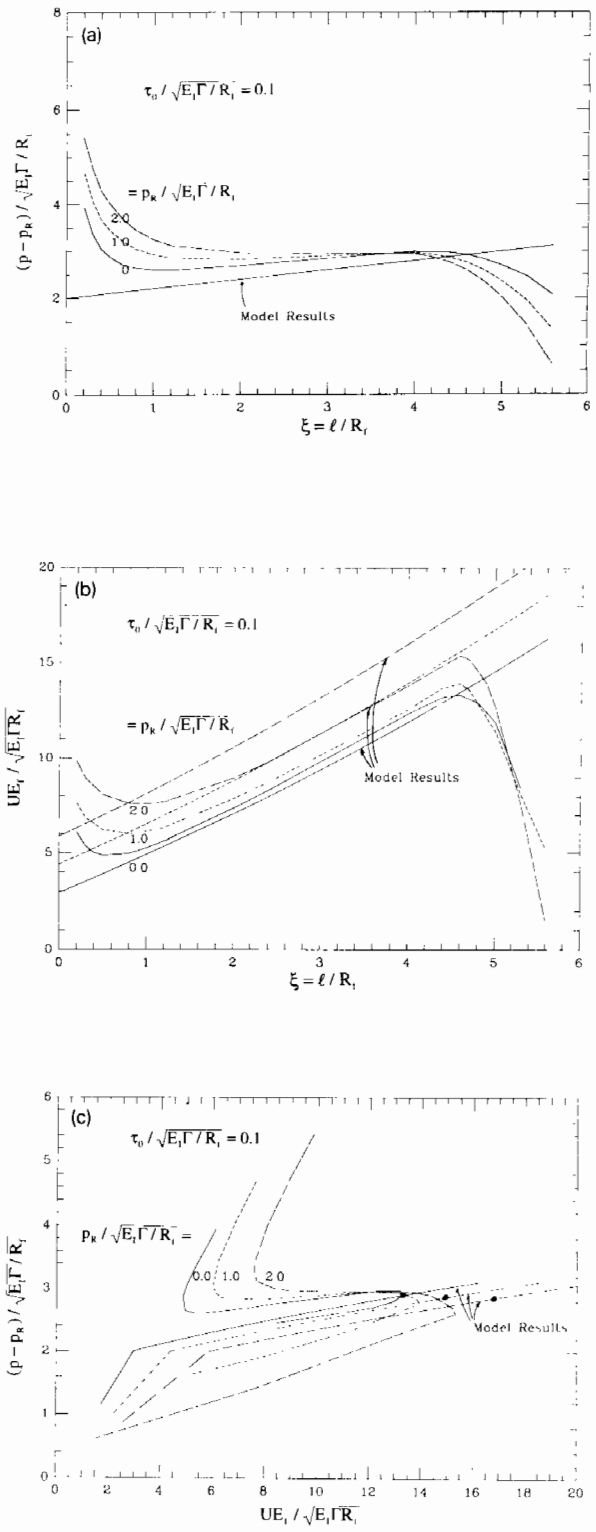

Fig. 8. Pushout behavior during the debonding phase for $\tau_0/(E_1\Gamma/R_f)^{1/2} = 0.1$ with several levels of residual axial compression p_R. Comparison of the full numerical results from (4.1) and (4.2) with the model predictions. In part (c) the point where $l = t - 1.5R_f$ is indicated by a dot for the model predictions. The parameters of the system are the same as those of Figs. 2–4 with $t/R_f = 6$, $E_f = E$ and $\nu_f = \nu = 1/3$.

Suppose for the purpose of discussion that the displacement U (rather than the load) is prescribed by the pushout device. Any loading device compliance could be taken into account in the following discussion, but a stiff device is well modeled by prescribing U. The straight line emanating from the origin in Fig. 7c is the load–displacement response of the system prior to attaining the debonding condition $K = K_c$. If a debond crack of length greater than about one fiber radius pre-exists, then the dashed line segment will intersect the debonding curve at a point such as A, and debonding will then progress smoothly as U is increased. If, however, the initial debond flaw is shorter than about one fiber radius, debonding will start at a point such as B and will advance dynamically arresting when the load drops to the lower value at B′ associated with the prescribed U. Subsequently debonding will progress smoothly with increasing U until the limit point with respect to U is reached. Values at the limit point are denoted by (p^*, U^*), corresponding to the point where the debond crack becomes unstable and breaks through to the bottom of the specimen. The limit point is attained when the debond crack tip reaches a distance of about $1.5R_f$ from the bottom. (The values given by the model at which $l = t - 1.5R_f$ is indicated by a solid dot in Fig. 7c.) From Figs. 2a and 5, it can be seen that the instability point corresponds to the strong up-turn in the dependence of K on p. Note further that the two cases shown with nonzero τ_0 are stable under *prescribed load* almost to the same point as under prescribed U. In other words, friction stabilizes the debonding process until the point where the debond approaches the bottom of the specimen such that there is very little dependence of the breakthrough values, p^* and U^*, on the compliance of the loading device.

Plots of p and U as functions of ξ and p versus U are shown in Fig. 8 for examples where residual axial compression p_R in the fiber is present as well as constant friction. In this case the normalized value of $p - p_R$ has been used as the ordinate to bring out the fact that the main effect of residual axial compression is to simply require an extra push roughly equal to p_R. The model tends to underestimate p and overestimate U, but the errors in p^* and U^* are not more than about ten percent. The range of the nondimensional residual stress parameter chosen in Fig. 8, from 0 to 2, covers the feasible range of this parameter. Using (3.4), one can readily show that the fiber will debond by residual stress alone (i.e., poke out of the matrix) if

$$\frac{p_R}{\sqrt{E_1\Gamma/R_f}} > 2\sqrt{\frac{E_f}{E_1 B_2}}\,. \tag{4.3}$$

The collection of terms on the right side of this inequality is usually fairly close to 2.

5. Closing remarks

The detailed numerical analysis of some specific examples in Section 3 and 4 indicate that the model equations provide a reasonably accurate characterization even for a specimen as thin as $t/R_f = 6$, with errors of about 10% being typical. The accuracy of the model predictions in the vicinity of the instability point is seen in Figs. 7 and 8 to be somewhat better than in the beginning stages of the debond process. As discussed in Section 3.4, the accuracy will be even better for thicker specimens. The detailed analysis indicates that the instability point in the debonding phase occurs when the debond reaches a distance of about $1.5R_f$ from the bottom of the specimen, and the model equations (2.17) and (2.18) can be used to predict this point. Moreover, as long as there is some friction, this instability point is not a strong function of the compliance of the pushout device. The instability is primarily associated with the strong upturn in the relation of K versus debond length seen in Figs. 2a and 5 as the debond crack approaches the bottom of the specimen.

A few remarks are in order in connection with use of the model equations of Section 2 to infer interface properties such as Γ and frictional characteristics from experimental pushout records. Firstly, one should be cognizant of the approximate nature of the model equations in making efforts to fit the model equations to ex-

perimental pushout data. The level of error reflected by the examples in Figs. 7c and 8c is typical for relatively thin specimens. Secondly, one must be aware that it may not be possible to distinguish between a constant friction characterization and a Coulomb friction characterization if the specimen is relatively thin. To see this, consider the frictional contribution to the pushout stress in (2.13). If ζ never exceeds $1/3$, say, then $e^{\zeta} - 1$ can be approximated by ζ and

$$\frac{\tau_0 + \mu n_R}{\mu B_1}(e^{\zeta} - 1) \cong 2(\tau_0 + \mu n_R)\frac{l}{R_f}. \qquad (5.1)$$

The combination $(\tau_0 + \mu n_R)$ is equivalent to an effective constant friction. In other words, if $\zeta < 1/3$, there is negligible 'Poisson effect' and the Coulomb friction contribution remains essentially unchanged at μn_R during the debonding phase. These remarks also apply to the pushout phase governed by (2.19), although note that the term $-\mu B_1 p_R$ does affect the Coulomb contribution relative to the debonding phase (5.1) in a way which does distinguish it from constant friction. Since the debond length is at most t, the condition that ζ never exceeds $1/3$ is simply $t/R_f < 1(6\mu B_1)$, which, depending on specific values of the parameters of the system, could be as large as 10 or more.

Equation (2.13) can be used to assess the relative importance of debonding toughness, residual axial stress, and friction to the pushout stress during the debond phase. As emphasized earlier, according to the model the residual compression in the fiber p_R simply adds to the required pushout stress. The terms

$$2\sqrt{\frac{\Gamma E_f}{B_2 R_f}}, \quad \text{and} \quad \frac{\tau_0 + \mu n_R}{\mu B_1},$$

each have dimensions of stress and, respectively, govern the debonding and frictional contributions. The nondimensional frictional parameter and residual stress parameter introduced in Section 4 used the first of the above quantities in their normalization. Thus, the relative importance of the contributions can be assessed from the relative magnitudes of these terms.

Finally, we wish to call attention to the fact that the relative slip u of fiber to matrix at the top of the specimen is only a tiny fraction of the fiber radius at break-through in many systems. This statement follows from inserting values for typical systems in (2.16) and from experimental records of pushout tests published in the literature. Thus, for example, a thin specimen with a fiber of radius 50 microns may undergo debonding with relative sliding u never exceeding a small fraction of a micron. If the asperity roughness has a wavelength which is long compared to u (which is the case for some fibers), then debonding does not involve the asperities sliding past one another. In fact, under these conditions, debonding will occur prior to the unseating, or unkeying, of the fiber asperity pattern from the matrix which surrounds it. The role of surface morphology during debonding under these conditions is not well understood, and it is not at all clear that a phenomenological friction law such as (2.1), whether for constant or Coulomb friction or some combination, should apply both to the debonding phase *and* the pushout phase after sliding distances on the order of the asperity wavelength have occurred. By the same token, frictional characteristics inferred from pushout tests where 'large' amounts of sliding occur may not be relevant for debonding and sliding under pullout conditions experienced in cracking applications for brittle matrix composites which involve small amounts of sliding.

Acknowledgement

The authors would like to thank A.G. Evans and D.B. Marshall for helpful discussions during the course of this work. The work was supported in part by the DARPA University Research Initiative (Sub-Agreement P.O. #VB38639-0 with the University of California, Santa Barbara, ONR Prime Contract N00014-86-K0753, the Materials Research Laboratory (Grant NSF-DMR-89-20490) and the Division of Applied Sciences, Harvard University.

References

Gao, Y-C., Y-W. Mai and B. Cotterell (1988), Fracture of fiber reinforced materials, *J. Appl. Math. and Phys., (ZAMP) 39*, 550–572.

Hutchinson, J.W. and H.M. Jensen (1990), Models of fiber debonding and pullout in brittle composites with friction, *Mech. Mater. 9*, 139–163.

Hutchinson, J.W. and Z. Suo (1991), Mixed mode cracking of layered materials, in: J.W. Hutchinson and T.Y. Wu, eds., *Adv. Appl. Mech. 29*, Academic Press, pp. 63–191.

Jero, P.D. and R.J. Kearns (1990), The contribution of interfacial roughness to sliding friction of ceramic fibers in a glass matrix, *Scripta. Metall. 24*, 2315–2318.

Kallas, M.N., D.A. Koss, H.T. Hahn and J.R. Hellmann (1991), On the interfacial stress state present in a "thin-slice" fiber push-out test, *J. Mater. Sci.*, to be published.

Kearns, R.J. and T.A. Parthasarathy (1991), Theoretical analysis of the fiber pull-out and push-out tests, *J. Am. Ceram. Soc. 74*, 1585.

Mackin, T.J., P.D. Warren and A.G. Evans (1992), Effects of fiber roughness on interface sliding in composites, Materials Department Report, University of California, Santa Barbara, to be published.

Marshall, D.B. (1992), Analysis of fiber debonding and sliding experiments in brittle matrix composites, *Acta Metall. Mater 40(3)*, 427–442.

Meda, G., S.F. Hoysan and P.S. Steif (1991), The effect of fiber Poisson expansion in micro-indentation tests, to be published.

Shetty, D.K. (1988), Shear-lag analysis of fiber pushout (indentation) test for estimating interfacial friction stress in ceramic-matrix composites, *J. Am. Ceram. Soc. 71*, C-107–C-109.

Takaku, A. and R.G.C. Arridge (1973), The effect of interfacial radial and shear stresses on fiber pull-out in composite materials, *J. Phys. D, Appl. Phys. 6*, 2038–2047.

Appendix

The numerical results have been obtained using a finite element code ABAQUS (Hibbitt, Karlsson & Sorensen, Inc., Providence, Rhode Island, USA) with eight-noded quadrilateral axisymmetric elements. The finite-element mesh consists of 1169 to 1305 elements. Mode 2 cracks of length l are assumed to exist along the interface. Since there is a square root singularity in the strain and stress fields at the crack tip, quarter-point elements are employed in the region nearest to the tip. The radial length of the smallest and largest elements are $1.01 \times 10^{-3}\ R_f$ and $1.60 \times 10^{-2}\ R_f$, respectively. For each pre-selected l, the energy release rate, G, is calculated using a J-integral option in ABAQUS. The contour selected to calculate G lies within the immediate vicinity of the tip, where the plane strain conditions are asymptotically approached. The calculation is performed for debond ratios ranging from $1 < l/R_f < 6$, with between twelve to twenty ratios used for a given specimen. The stress intensity factor K and the average downward displacement of the end of the fiber U are also calculated. The displacement U is obtained by averaging the nodal axial displacement of the fiber end over the intersection area of the fiber, while the relative displacement u is obtained by subtracting the average axial displacement of matrix from U. Since the linear elastic behavior is assumed, the contributions to K and U from the applied compression p, the residual axial stress p_R and constant friction τ_0 along the interface could be calculated separately as discussed in Section 3. The contribution due to axial residual compression p_R in the fiber is modelled by applying a uniform tension p_R to the fiber ends, and a compressive stress $\rho p_R/(1-\rho)$ acting over an annular region whose radius extends from R_f to $R_f/\sqrt{\rho}$ on both the top and bottom faces of the specimen. The finite-element results for the constant friction case are obtained by applying an appropriate concentrated shear force to each nodal point along the crack faces such that an equivalent uniform shear stress τ_0 is achieved.

Errata for Hutchinson and Jensen (1990)

Equation (24): $c_2 = \frac{1}{2}a_2(b_2 + b_3)^{1/2}$,
Equation (47): k_1 should be replaced by $k_1/(1 + k_1)$,
Equation (59): e^{ζ_1} in the numerator should be replaced by $e^{-\zeta_1}$.